

Chapter 1

Laser-Assisted Scanning Probe Alloying Nanolithography (LASPAN)

Luohan Peng^{*}, Huiliang Zhang[†], Philip Hemmer, and Hong Liang

Abstract Nanoscale science and technology demands novel approaches and new knowledge for further development. Nanofabrication has been widely employed in modern science and engineering. Probe-based nanolithography is a common technique to manufacture nanostructures. This research contributes fundamental understanding in surface science through development of a new methodology. A delicate hardware system was designed and constructed to realize the nanometer-scale direct writing. A simple and unique process, namely, laser-assisted scanning probe alloying nanolithography (LASPAN), to fabricate well-defined nanostructures has been developed. The LASPAN system, process, and the application in gold-silicon (Au-Si) binary system have been discussed in this chapter.

1.1 A Brief Review of Scanning Probe-Based Nanolithography

1.1.1 Introduction

Lithographic technologies have been playing a critical role in modern nanoscale science and engineering. Optical lithography is a typical top-down approach where prepatterned fine structures are fabricated with precise control [1, 2]. Molecular self-assembly process well represents the bottom-up approach, where very fine nanostructures are created [3–8].

^{*}Currently at Applied Optoelectronics, Inc.

[†]Currently at Harvard University.

Scanning probe microscope (SPM) was invented in the early 1980s, and it has been widely used in many disciplines of science and engineering [9–11] ever since. A tiny sharp probe, with tip radius usually ranging from 15 to 50 nm, is used in scanning probe microscopes. In recent years, it has been realized that atomic interaction between the scanning probe and interrogated sample surface is not only useful for nanoimaging but can also be utilized for revolutionizing nanofabrication approaches, including nanomanipulation, nanopatterning, and nanodeposition. The nature of the sharp probe suggests that SPM be employed as a potential tool in both constructive and destructive nanolithographic approaches [12–15]. The SPM-based nanofabrication processes offer unique advantages of high resolution and registration accuracy, in vivo inspection capability readily available, process automation with computer control, and low-cost process under ambient conditions. Mass production is also possible with large scanning probe arrays [16–18]. For material deposition and patterning, a popular SPM-based technique named dip-pen nanolithography (DPN) has been developed [12, 19, 20]. With the sharp scanning probe tip, DPN can directly dispense a wide variety of solution-based chemicals onto a substrate surface to create single or arrayed nanoscale pattern or structures [21–23]. The effectiveness of DPN relies on the material transfer from the probe tip to the substrate surface via the water condensation existing in between [24, 25]. However, this requirement creates a limitation in the fabrication of metallic nanostructures due to the insolubility of metals in water and many other solvents.

1.1.2 Laser-Assisted Process

Laser-assisted processes have been widely applied in nanomanufacturing [26]. These processes include laser-assisted micro-/nanomachining; laser-assisted materials synthesis and modification (deposition and removal); and laser-assisted nanopatterning. Pulsed lasers are primarily used in the processes. Compared to other nanofabrication techniques, such as electron beam lithography, laser-assisted lithography has the advantage of high precision, simple setup, and high yield [27]. Pulsed lasers have been used to enhance the nanoimprint lithography process, in which the polymer film is heated by the pulse laser, occurring simultaneously with imprinting [28]. The scanning probe microscope (SPM), combined with pulsed laser irradiation, provides a novel means to realize nanopatterning. The mechanism of the SPM-pulsed laser processes can be rather complicated [29, 30].

1.1.3 Stimulated Nanoalloying and Nanocrystallization

In the scope of this research, nanoalloying is defined as the process through which two elements are mixed in order to form an alloy at the atomic or nanometer scale. During this process, solid crystals can be generated from a uniform solution with the

aid of certain external stimulations such as mechanical force and heat. We define this solid crystal formation as nanocrystallization. In most nanomanufacturing processes, nanoalloying and nanocrystallization are commonly involved when materials are in contact, i.e., where an interface is formed.

When two different types of elements (metal or nonmetal) are mixed, under external mechanical and thermal stimulations, nanoalloys can be synthesized. These nanoalloys have exhibited enhanced properties [24, 25, 31].

To summarize, we have reviewed the existing nanomanufacturing processes by which various nanostructures can be fabricated. Scanning probe-based nanolithography is a promising approach to generate ultrasmall features, due to the nature of the sharp probe. With the aid of external mechanical and thermal stimulation, nanoalloying and nanocrystallization processes are present.

In this chapter, the configuration of LASPAN system which integrates a continuous wave (CW) laser into an atomic force microscope (AFM) is firstly shown. Then, a simplified SPM-laser fabrication process is completely developed, where direct nanolithography is realized. Last, an application of this AFM-based nanolithography process is demonstrated in gold and silicon binary materials system.

1.2 LASPAN System Configuration

1.2.1 AFM Writing at Room Temperature

The writing experiment with a stand-alone AFM at room temperature, namely, scanning probe alloying nanolithography (SPAN), has been previously reported [32]. The materials system employed in this research consists of a single crystal silicon substrate and gold-coated silicon nitride probes. In the SPAN process, it was proposed that the induced stress during writing would be a governing factor to form nanostructures. After repeating numerous room temperature writings, we found that the localized thermal energy input, which is the heat generated by friction, also played an important role in the alloying process. Hence, a new sample stage with a built-in electric heater was designed and manufactured. The sample mounted on the stage can be heated up to 300°C. The diagram of the system with this heating stage is shown in Fig. 1.1.

1.2.2 Laser System Attachment

The heating stage provides a good deal of thermal energy to the substrate during writing. The sample is heated through thermal conduction. However, the piezoelectric sensor in the AFM scanner is integrated behind the tip mount and is highly sensitive to external thermal interference. The critical temperature is approximately

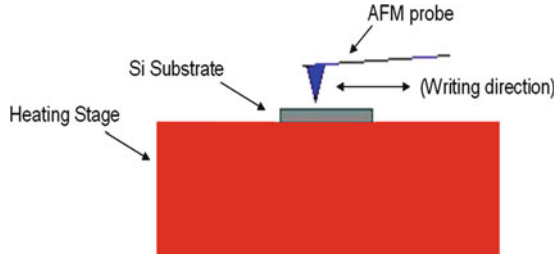


Fig. 1.1 AFM setup for SPAN with implement of heating stage

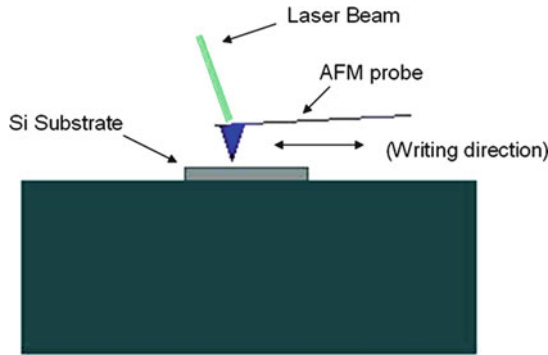


Fig. 1.2 AFM setup with implement of laser system

150°C (according to the manufacturer, PNI Inc.). When the tip comes in contact with the substrate, the scanner is less than 1 mm away from the heat source. Therefore, the system cannot function correctly once the substrate is above the critical temperature.

In general, the alloying process during writing requires significant thermal energy input into different binary materials systems. The heating stage setup can only provide a limited thermal environment without damaging the AFM system. An external laser system was introduced to tackle this problem.

An Nd:YAG solid-state laser (532 nm) was selected to be integrated into the AFM setup, referred to as the laser-assisted scanning probe alloying nanolithography (LASPAN) system (Fig. 1.2). The laser beam was directly projected onto the backside of the AFM cantilever to provide thermal energy. There are two main advantages of the laser optical system: First, the laser provides highly controllable power output. The maximum output power of the laser in free space is 65 mW. By inserting a double spin attenuator (one spinner's selection ranges from 0.0001 to 0.1; the other one ranges from 0.14 to 0.63), we can easily decrease the laser power output to different desired levels. Second, the heating spot is highly localized. The diameter of the output laser beam spot can be focused to about 10 μm by the objective lens. This tightly focused laser beam spot can provide highly localized heating without interfering in the piezoelectric sensor in AFM.

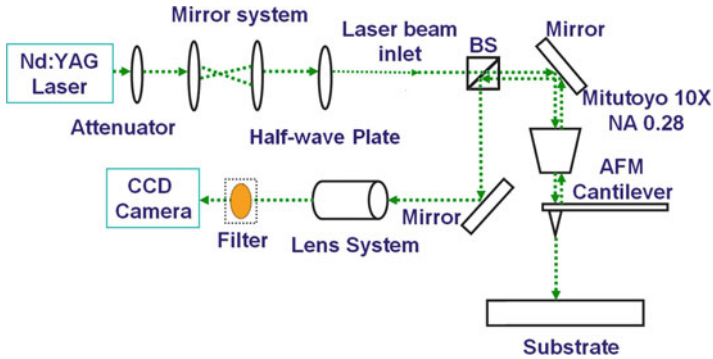


Fig. 1.3 Diagram of integrated laser optical system and Nano-R2 AFM

1.2.3 Integration of Laser and AFM Systems

Initially, an optical fiber was used to direct the laser beam out, due to the convenience of it being commercially available. However, it was found that the laser beam was rather difficult to align through the fiber. In addition, the intensity of the laser beam was significantly decreased by about 70%. These two drawbacks prevented using the optical fiber. To address these issues, the free space setup is then implemented. The double spinner attenuator is set right next to the laser beam emitter to coarsely adjust the laser power output. Four mirrors were used to align the laser beam's height in the free space. A half-wave plate cascaded with an optical polarizer is inserted after the mirror system to finely adjust the laser power output. All parts are mounted on a sizeable breadboard laser desktop by magnetic bases. A number of stainless steel cylindrical posts are used to increase the vertical displacement of the laser optical system, in order to align the laser beam into the AFM system.

The maximum output power after attenuation of this laser optical system is 30 mW, while one can finely tune the output laser power as precise as $0.1 \mu\text{W}$. Every mirror sits inside mirror mounts with two separate control knobs; each of them provides either horizontal or vertical displacement of the mirror. This displacement reflects the laser beam spot projected to the backside of the probe cantilever. Overall, this optimized optical system has the ability to manipulate the laser power output and the position of laser beam spot in a highly controllable fashion.

The Nano-R2 AFM has its own optical system, which is mainly used to observe the sample and find the point of interest (POI). The illuminator can be taken out of the whole setup, leaving a hollow channel. This open channel is a perfect interface to connect laser optical system and the AFM. The aligned laser beam enters the microscope through the channel, is incident on a beam splitter (BS), and is split by into two beams. One beam goes through the objective and is eventually focused on the cantilever; the other beam is reflected back and filtered out to prevent the CCD camera screen from damage. The complete diagram can be found in Fig. 1.3.

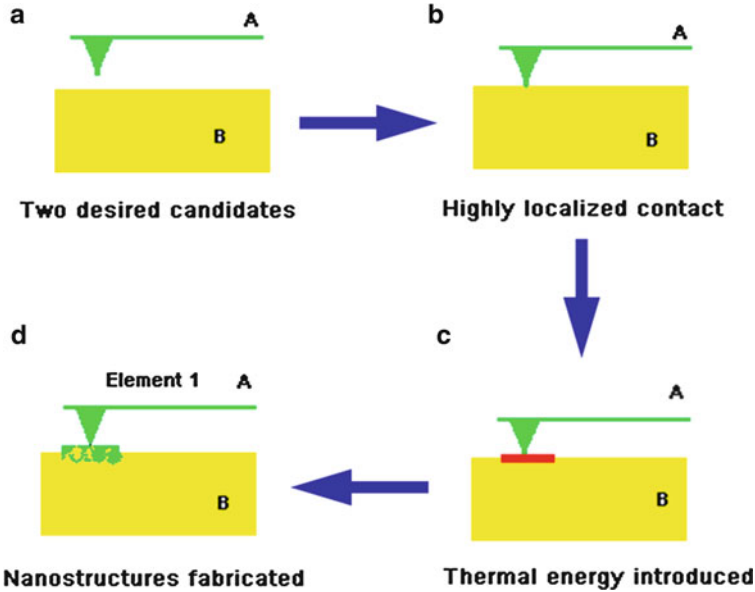


Fig. 1.4 Fundamental diagram of LASPAN process

1.3 LASPAN Processes and Applications

1.3.1 Principles of LASPAN Process

As the name indicates, the LASPAN technique has two major components, i.e., laser-assisted process and scanning probe microscope (SPM)-based writing. The fundamental principles of LASPAN are to generate a highly localized interface (at nanometer length scale) between two preselected material candidates, control the alloying process by triggering external mechanical and thermal energy input, and fabricate nanostructures in the defined region. A diagram of the basic LASPAN process is shown in Fig. 1.4.

The LASPAN technique developed here is based on an atomic force microscope (AFM), which has been actively used in many areas of nanotechnology since its invention. An AFM can be used not only as a morphology characterization instrument but also as a processing tool. One standard function of our AFM (PNI, Nano-R2) is the control of tip scanning. With the aid of software, the tip can be replaced to anywhere on the sample surface, and perform a raster scan. The radius of the curvature of a sharp AFM tip generally ranges from 15 to 50 nm. The tip is naturally utilized to provide a highly localized interface, when it is brought into contact with the substrate. Once the tip is in place, the laser spot is introduced on the backside of the probe. The thermal energy is absorbed by the cantilever and tip, which results in a local temperature increase in the interface. To summarize, there

are three major challenges when developing the LASPAN process: (a) cross-linking between AFM and laser system, (b) mechanical stress load, and (c) thermal energy input. To overcome such challenges, a systematic approach with high precision is required. The details of the LASPAN process are discussed in the following sections.

1.3.2 Optimization of LASPAN Generic Process

The LASPAN experimental procedure has four major parts: (a) AFM optimization, (b) stress loading-bending of cantilever, (c) external laser integration optimization, and (d) writing. Each part is described in detail as follows.

1.3.2.1 AFM Optimization

The Nano-R2 AFM must be optimized before writing is started. The substrate and precoated probe are first mounted on the sample puck and tip holder. The scanner linearization is then performed automatically by the AFM controller, once a command is sent to the AFM computer. The configuration is loaded as “contact mode.”

The tip we use in LASPAN is different from those used in normal contact mode imaging. We purposely chose the silicon nitride (Si_3N_4) cantilever without a backside metal coating layer that would prevent a heavy reflection loss of incoming laser intensity. Hence, the reflectivity of this type of cantilever is fairly low (estimated value approximately 15% or less). On the other hand, the power of the AFM’s internal laser is low (around 1 mW). In most cases, the reflected signal of the pure Si_3N_4 cantilever is too weak for the detector; thus, the detector is unable to sense the signal and give correct feedback. Therefore, we must manually adjust the tip position, which is one drawback of using pure Si_3N_4 cantilevers. During the whole LASPAN process, the internal laser beam remains off.

The optical system of the AFM observes in situ movement of the probe. We first use the objective lens to focus on the tip, record the z-position, then focus on the substrate, and record the z-position again. The software automatically calculates the distance between the measurements and drives the scanner to guide the tip’s coarse approach to the sample surface. After the coarse approach is completed, both the AFM tip and sample surface are in the depth of field of the objective. The XY piezoelectric stage then moves the substrate in the xy plane until the designated position appears on the screen and the tip falls into the referenced area.

The last step in AFM optimization is to initialize the line scan. The scanning parameters, such as length (μm), frequency (Hz), and scanning angle, should be entered before scanning. Once the parameters are set, we run the line scan a few times. The system will automatically find the initial point for the line scan, according to the value entered. Generally, there is horizontal displacement (up to $50\mu\text{m}$) between the physical tip position after the coarse approach and the initial line scan

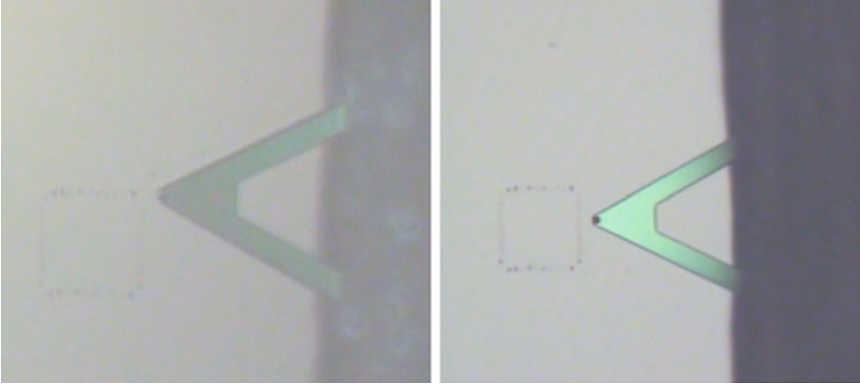


Fig. 1.5 Reflection change on the probe shows tip-surface engagement and clear bending. *Left*: before tip is in contact with surface; *Right*: after load is applied

position. The trial scans are important because they eliminate this displacement. The tip should be stopped at the left end point of the line scan, since this position will offer more room for laser spot focus in later processes.

1.3.2.2 Stress Loading-Bending of Cantilever

After AFM optimization, one wants to bring the tip into contact with the surface and apply the load to certain level. Since the feedback system is not engaged, a manual movement of the scanner downward toward the substrate is applied.

When the coarse approach is done, the distance between the tip and substrate is approximately 50–70 μm . Each step of the main control of the scanner's vertical displacement is 5 μm . The tip movement is monitored in situ by the AFM optical system at all times. The tip moves down until a clear bending appears (see Fig. 1.5), indicating that the tip is in close contact with the sample surface. The fine adjustment of the scanner can be realized by manually moving the tip down further at smaller displacement step. The smallest step is 160 nm. Alternatively, retracting the tip and pushing it down finalizes the “zero-load” tip position. Finding one particular empirical standard involves retracting (or lowering) the tip until the tip slippery occurs, then moving the tip back one step in the opposite direction. Once the tip is at “zero-load” position, the load is ready to be applied.

Starting from the “zero-load” position, the tip is lowered down until the desired load is reached. The load f_L is estimated through (1.1) as

$$f_L = k \cdot \Delta z \quad (1.1)$$

where k is the spring constant of the cantilever and Δz is the deflection of the cantilever, which is equal to the displacement of the tip from the “zero-load”

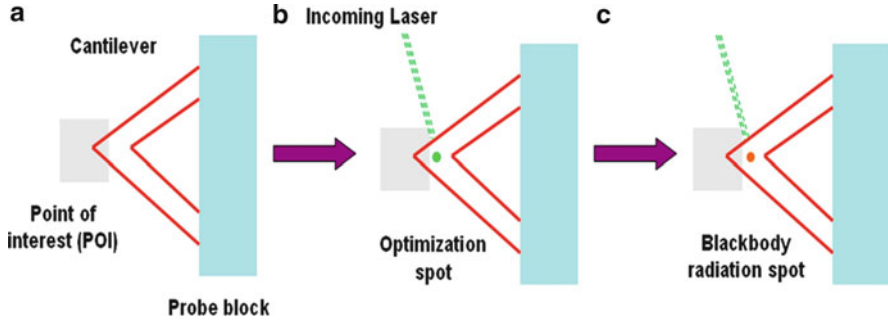


Fig. 1.6 Diagram of laser optimization. (a) Locate point of interest (POI); (b) laser spot optimization with attenuation and without filter, *green spot* is present on the backside of cantilever; (c) blackbody radiation spot optimization filtering out green laser, shiny flash spot is present indicating localized heating

position. The values for the spring constants of different cantilevers were given by the company (from 0.6 to 0.58 N/m), and Δz ranges from 1 to 15 μm ; thus, the load applied ranges from 0.6 to 8.7 μN .

1.3.2.3 External Laser Integration and Optimization

The third part of the LASPAN process is to optimize the external laser integration. After the stress is applied to the AFM probe, the scanner, the tip, and the sample will be fixed; only the optical components are manipulated. We need to systematically align the laser beam and make sure the focused laser spot projects to the right spot on the backside of the cantilever. The complete diagram of operations in this part is shown in Fig. 1.6.

The laser beam is introduced into the AFM optical system through the open inlet path (shown in Fig. 1.7), where the AFM illuminator was pulled out. The double spinner attenuator is set at maximum attenuation (about 1/1,000,000). Thus, the output laser beam is too weak to damage the CCD camera. A green spot appears on the screen, indicating the laser beam's current position. The objective integrated into the AFM can be moved in a horizontal plane by two attached screws. While the objective moves, the green spot stays at the same position. The screen displays the tip moving back and forth to approach the green spot. The mirrors are sometimes employed to finely adjust the absolute position of the green laser spot to align it along the cantilever's axis. The manipulations of objective and mirrors are utilized to land the spot on the cantilever.

A filter is inserted in front of the CCD camera after the green spot is located (refer to the diagram in Fig. 1.3). This filter allows only laser beams with a wavelength greater than 600 nm to pass. Hence, the green laser beams resulting from the Nd:YAG laser will not damage the CCD camera when the laser power is tuned up. At this stage, the external laser is engaged to provide thermal energy

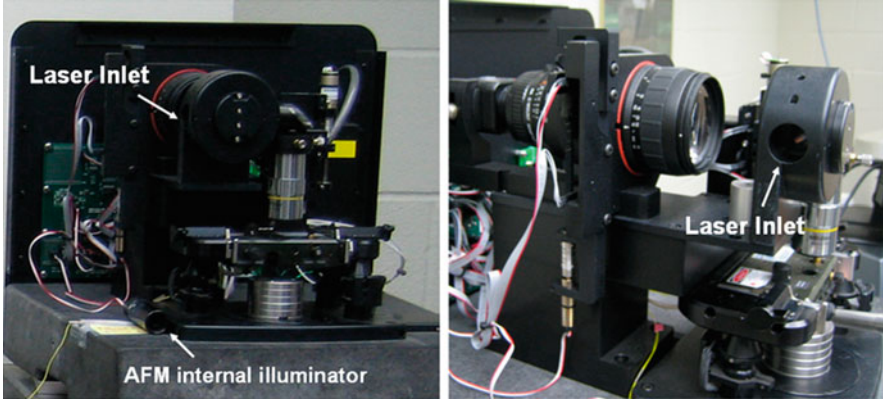


Fig. 1.7 Connection between laser and AFM. *Left*: front view of laser inlet; *Right*: side view of laser inlet

input. The objective focuses the laser beam down to $10\ \mu\text{m}$, and the maximum output power when reaching the cantilever is 30 mW. The power intensity can be expressed as

$$I = \frac{P}{\pi \cdot (D/2)^2} \quad (1.2)$$

where I is the power intensity, P is the output power of laser beam, and D is the diameter of the focused laser beam. Plugging the numbers above into (2), we can calculate the value of I as $3.9 \times 10^8\ \text{W/m}^2$. This intensity is enough to provide localized heating up to several hundred degrees.

Experimentally, when the laser beam hits the cantilever, the focused spot rapidly heats up. Hence, the heated area will irradiate the light at a certain wavelength (usually between 600 and 750 nm, as a result of incoming laser power control) in all directions. One of the irradiated light waves is sensed by the optical setup and arrives at the CCD camera after passing through the filter. A shining spot is then displayed on the screen, which reflects the real “heated-up” spot on the cantilever.

In the LASPAN process, we measure the laser power by a power meter (ThorLabs). The direct laser output power is 60 mW, and the AFM optical system with beam splitter and objective has a 50% energy loss; hence, the maximum real laser output power applied on the tip is 30 mW. Then, the double spinner attenuator generally reduces it to about 12 mW. Finally, the polarizer cascaded with the half-wave plate finely tunes it down to the desired power output. The fine-tuning can be as accurate as 0.01 mW.

We often use 10 mW laser power output to find the flashing spot on a screen, followed by the cantilever’s alignment. The final position of this flashing spot should be along the center axis of the probe, and at $X\ \mu\text{m}$ (line scan length) away from the projection of the sharp tip on the cantilever. Experimental images are found in Fig. 1.8.

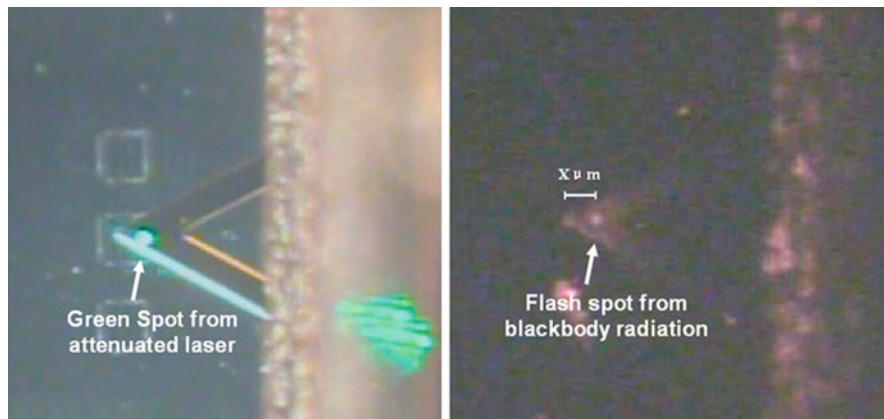


Fig. 1.8 Experimental images during laser optimization. *Left*: green spot on cantilever, after position optimization; *Right*: flash spot from blackbody radiation on cantilever, after position optimization

The optimization of applied thermal energy consequently decreases the laser's output power. A piece of paper is frequently used to block the laser beam, because the high-power laser beam might burn out the tip itself. We also need to pay attention to the alignment of the flashing spot, a process which should be completed as quickly as possible. The longer it takes, the more damage will be inflicted on the probe. Usually, this process is completed within 30 s. Most of the time, an external illuminator is needed to provide illumination to the sample in order to aid in alignment.

1.3.2.4 Nanowriting Process

After the laser beam's optimization, we block the laser beam with a piece of paper. A timer is employed to set up the duration of the writing. Then, the paper is removed as both the line scan and the timer immediately commence.

In the LASPAN writing, the AFM probe scans back and forth on the sample surface in a designated area, with a laser spot simultaneously focused on the backside of the cantilever. The laser spot is at a fixed position, but the probe is raster scanning over the sample surface. Due to the integration of both systems, it is difficult to synchronize the laser spot and tip. However, this does not really affect the thermal energy input, since the size of the whole probe is comparable to that of focused laser spot.

When the writing is finished, the line scan is manually stopped, and immediately, the laser beam is blocked by the attenuator. Then, the tip is retracted from the surface by moving the scanner up little by little until it clears the contact area. The objective and scanner are then brought back to their original positions. The filter is removed and the internal AFM illuminator is inserted. We then document the values of three

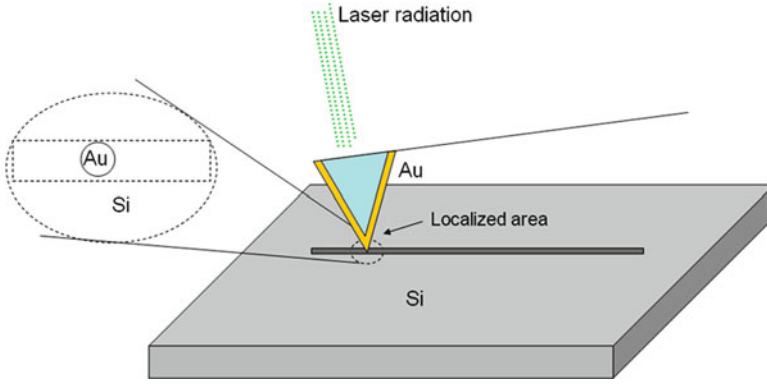


Fig. 1.9 A schematic drawing showing Au-Si interface in the LASPAN process

raster writing parameters: the writing time period t (s), line scan length l (μm), and scan frequency f (Hz). Then, the number of strokes N and the writing speed v ($\mu\text{m/s}$) can be derived as

$$N = f \cdot t \quad (1.3)$$

and

$$v = \frac{2f \cdot l}{t} \quad (1.4)$$

Steps (a) to (d) (as in Fig. 1.4) form a complete cycle of the LASPAN process.

1.3.3 LASPAN in an Au-Si System: A Case Study

A gold(Au)-silicon(Si) system has been chosen to deploy the LASPAN process, due to the fact that a reasonable low eutectic temperature can be reached in this binary material system. The LASPAN undergoes a mechanical and thermal process simultaneously (diagram shown in Fig. 1.9). Understanding the energy generation and the path of dissipation is important for advancing the LASPAN technique. In this section, the morphology of the substrate after the LASPAN process is demonstrated, while a number of experiments were carried out under various experimental conditions. In fundamental aspects, a Rutherford backscattering spectrometry (RBS) analysis was carried out to investigate the material transfer.

1.3.3.1 Morphology on Substrate After LASPAN

A number of experimental trials were carried out, among which, 25 writings were found effective in generating nanostructures. A matrix based on recorded data was constructed, as shown in Table 1.1. The first four columns are the different values

Table 1.1 LASPAN writing matrix

# of Strokes	Laser power (P , mW)	Speed (v , $\mu\text{m/s}$)	Load (ΔZ , μm)	Line
200	4.5	24	3	G
200	5.5	60	10	G
100	5	56	10	G
90	5	30	9	G
60	0	60	15	G
200	5	60	3	N
200	5	32	10	N
200	4	32	10	N
50	5	36	1	N
200	8	32	10	P
200	7.5	32	10	P
200	7	32	10	P
200	6	32	10	P
42	8	3.2	15	P
54	6	3.2	15	P
42	5	3.2	15	P
42	7	3.2	15	P
150	5.5	36	3	Y
150	5	60	5	Y
100	6	48	3	Y
84	4.5	14	15	Y
84	5.5	14	15	Y
60	4.5	60	15	Y
90	5.5	30	9	Y
100	5	52	14	Y
100	5	15	4	Y

of those four key parameters used during the experiments: number of strokes, laser power, speed, and load. The fifth column is the topography result, and the abbreviations represent the following: “G” – grooves; “N” – nonvisible structure; “P” – polished line trace; and “Y” – line-like nanostructure (above surface).

The polished line traces are created because of either excessive thermal energy (higher laser power than needed) or extra number of strokes; the grooves are present if too much mechanical load is applied (load is too high); nonvisible structures are found are due to various reasons, such as small load or low writing speed. However, according to the matrix, we observe that the LASPAN process is not dominated by a single factor, but by the synergy of all four key parameters.

The LASPAN process modifies the substrate surface in four different categories: nonvisible structures, polished line traces, grooves, and line-like nanostructures. Obviously, the last one represents the most favorable result of this technique. We demonstrate topography images in sequence:

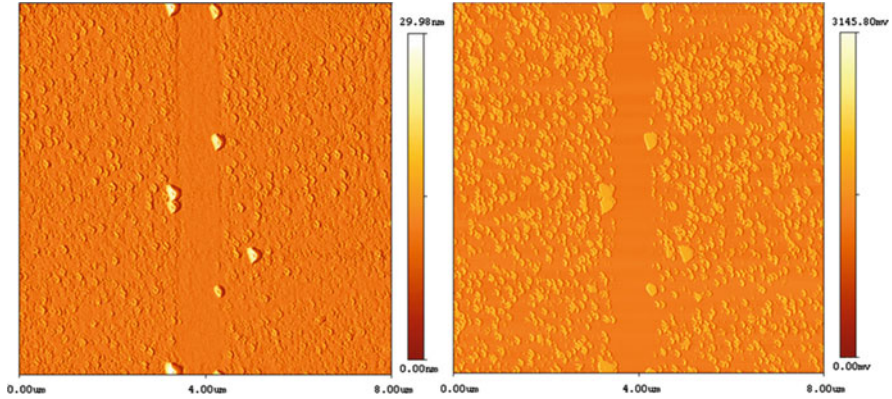


Fig. 1.10 2D image of a polished line track. *Left*: height image; *Right*: phase image

- (a) Nonvisible structures: No significant change of morphology of the same scanning area before and after writing. The images are not shown since there are no observable nanostructures.
- (b) Polished line trace: A line trace follows the tip movement, and the width of the line trace is much larger than the tip radius (usually < 100 nm for a newly coated probe). More importantly, the roughness within the trace is one order lower than the original surface. The height and phase images are shown in Fig. 1.10. The whole scanned area is $8\text{ }\mu\text{m}$. A clear polished trace is found in the center of the image. The overall roughness of the surface is 29.98 nm , but the selected area inside the polished line trace has a roughness of 0.99 nm . This means that the line trace was polished when the AFM probe scanned over.
- (c) Groove line traces: A line trace that follows the tip movement, with the width of the line trace being comparable to the tip radius. The scanned area is lower than the original surface, and the topography is literally a groove. The height and phase images are shown in Fig. 1.11. The whole scanning area is $10\text{ }\mu\text{m}$. A clear groove line trace is found in the center of the image. The entire track is straight, and the line width remains uniform throughout. In this category of results, the AFM tip plows the surface during writing.
- (d) The last category of the LASPAN process, as we expected, is a line-like nanostructure. We define the line-like nanostructure as a line trace which follows the tip movement, with the width of the line trace being comparable to or less than the tip radius. The fabricated structure has a certain height above the original surface. The topography is a line-like nanostructure or, more precisely, a nanobelt. The height and phase images are shown in Fig. 1.12. The whole scanning area is $18.7\text{ }\mu\text{m}$. A clear line trace is found in the center of the image. It is found that the width and height of the line-like nanostructure are 52 and 0.55 nm , respectively. The total length of this line is $30\text{ }\mu\text{m}$. In this category of results, the AFM tip fabricates the nanostructure over the surface during the writing. The nanostructure is highly localized in the tip scanning area.

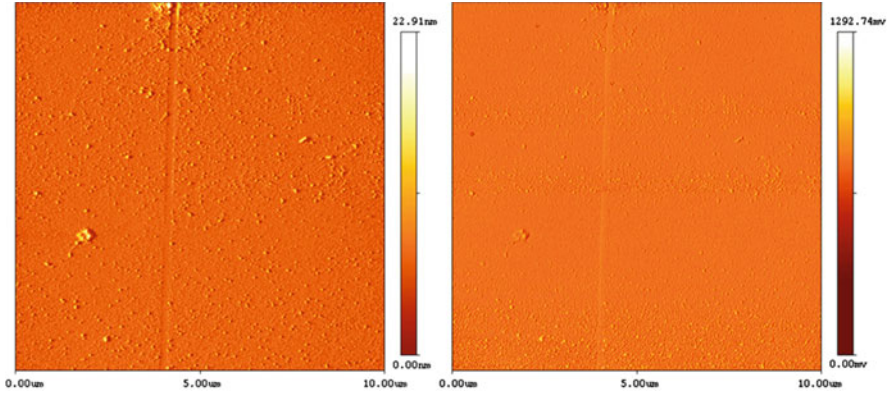


Fig. 1.11 2D image of a groove line track. *Left*: height image; *Right*: phase image

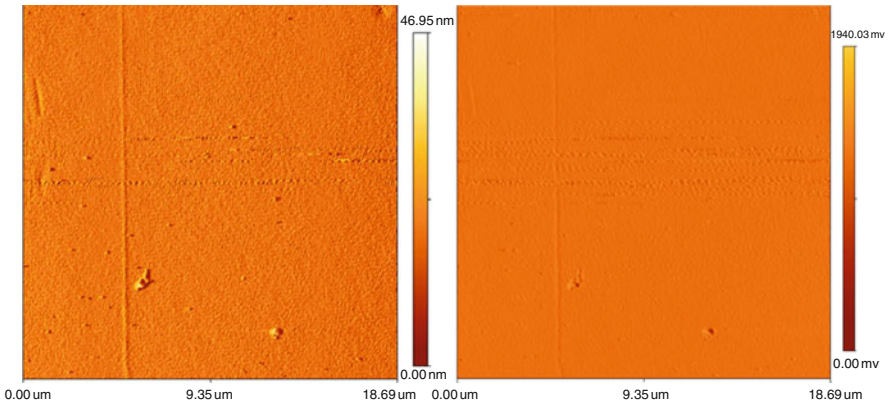


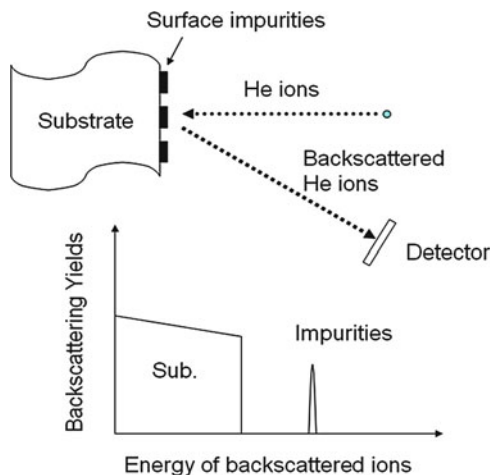
Fig. 1.12 2D image of a line track. *Left*: height image; *Right*: phase image

1.3.3.2 Rutherford Backscattering Spectrometry (RBS) Analysis

A key question to be addressed in our study is whether gold (Au) atoms are transferred from the tip to the silicon (Si) substrate. By conducting Rutherford backscattering spectrometry analysis, we obtained clear evidence of Au presence on the Si surface.

RBS analysis has been extensively used for accurate determination of film composition and surface contamination of solid-state targets. The technique was developed from the well-known “Rutherford scattering experiments.” The application of RBS technique in characterizing film composition is illustrated in Fig. 1.13. Basically, ions scattered from a sample’s surface have energy characteristics of the mass of target atoms. The ratio of energy of backscattered ions to incident ions is determined by the detecting angle, masses of target atoms, and projectiles.

Fig. 1.13 A schematic drawing of yield vs. energy for backscattered helium ion from a surface-engineered sample in Rutherford backscattering spectrometry (RBS) analysis



By measuring the energy of backscattered ions, we can tell the mass of impurities presented on the substrate surfaces.

RBS quantitatively determines the amount of surface atoms. The relative number of particles backscattered from a target atom into a given solid angle for a given number of incident particles is related to the differential scattering cross section. The scattering cross section is basically proportional to the square of the atomic number of the target atom.

RBS analysis was performed by using a 2.0 MeV helium (He) ion beam with a semiconductor detector positioned 165° away from the incident beam. The detector energy resolution was around 20 keV. The sample was a Si (100) wafer after sliding by an Au-coated Si_3N_4 probe. To maximize the Au signals in RBS spectrum, the sliding was continuously repeated on a preselected region. RBS analysis was limited to the marked region. The ion beam was accurately positioned by using a four-axis goniometer with accuracy of 0.01° in tilting and rotation, and 0.01 mm in translation. Figure 1.14 shows the RBS spectrum obtained. The inset shows an RBS peak observed at a channel of around 465. The peak position corresponds to the backscattering of He ions from the mass of Au atoms. Figure 1.14 also shows that the amount of Au detected was extremely small.

In Fig. 1.15, we compared the RBS spectrum and Rutherford backscattering spectroscopy analysis package, i.e., RUMP simulation. The red line is a fitting curve which assumes that Au atoms have an aerial density of 2.8×10^{13} atoms/cm² on the Si surface.

The RBS analysis provides clear evidence that Au is present on the sample surface through the LASPAN process. Therefore, in the process, an interface of gold and silicon is formed in the highly localized area which is defined by AFM tip dimensions. The RUMP simulation gives the aerial density of gold atoms in the fabricated nanostructures. This can be used to estimate the concentration of gold in the Au-Si nanostructures.

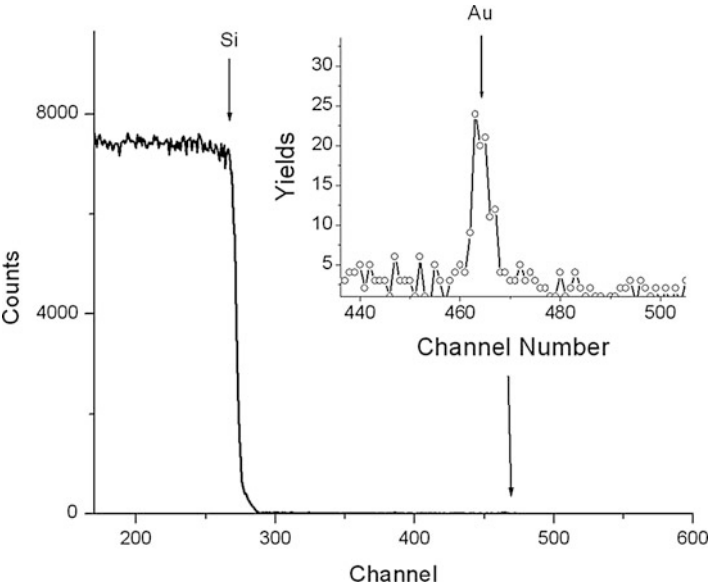


Fig. 1.14 RBS spectrum obtained from a Si (100) surface after sliding with an Au-coated Si₃N₄ probe

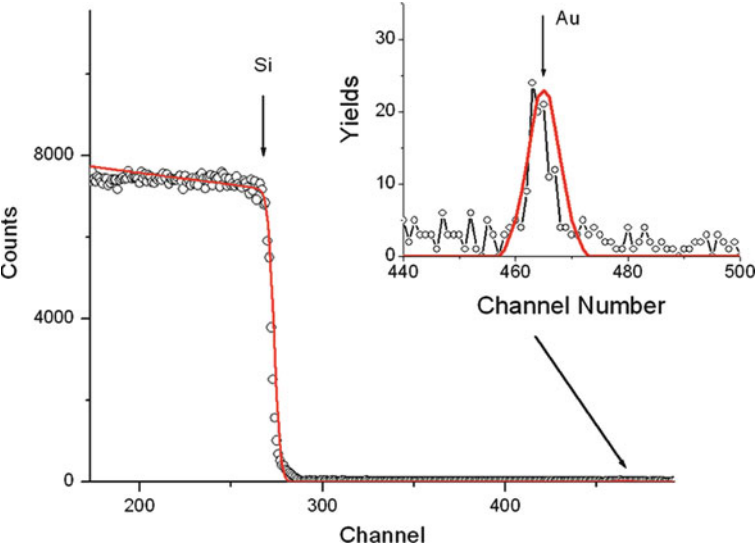


Fig. 1.15 Comparison between RUMP simulation and RBS spectrum for a (100) Si after sliding with an Au-coated Si₃N₄ probe

1.4 Conclusions

This research is focused on a novel nanofabrication process, i.e., laser-assisted scanning probe alloying nanolithography (LASPAN). An experimental setup in combinations of an existing atomic force microscope (AFM) and an external laser optical system has been designed and developed. The LASPAN process is then exercised and optimized in a simple eutectic binary system, i.e., gold-silicon (Au-Si) system. The RBS analysis clearly showed the materials transfer from gold-coated probe to the silicon substrate. Four aspects of nanostructures were produced through LASPAN process. Among them, a designated line-like nanostructure was fabricated under optimized condition. The LASPAN approach opens new areas of fundamental research in surface and materials science, and the technique developed in this work can potentially generate new ways to make nanodevices.

Acknowledgements This work was sponsored by the National Science Foundation (grant number 0506082).

References

1. R.C. Jaeger, *Introduction to Microelectronic Fabrication*, 2nd edn. Modular Series on Solid State Devices (Prentice Hall, Upper Saddle River, 2002)
2. M.J. Madou, *Fundamentals of Microfabrication: The Science of Miniaturization*, 2nd edn. (CRC Press, Boca Raton, 2002)
3. N.M. Miskovsky, T.T. Tsong, Field evaporation of gold in single- and double-electrode systems. *Phys. Rev. B* **46**(4), 2640 (1992)
4. J.I. Pascual, et al., Quantum contact in gold nanostructures by scanning tunneling microscopy. *Phys. Rev. Lett.* **71**(12), 1852 (1993)
5. G.S. Hsiao, R.M. Penner, J. Kingsley, Deposition of metal nanostructures onto Si(111) surfaces by field evaporation in the scanning tunneling microscope. *Appl. Phys. Lett.* **64**(11), 1350–1352 (1994)
6. D.H. Huang, T. Nakayama, M. Aono, Platinum nanodot formation by atomic point contact with a scanning tunneling microscope platinum tip. *Appl. Phys. Lett.* **73**(23), 3360–3362 (1998)
7. D. Sundrani, S.B. Darling, S.J. Sibener, Hierarchical assembly and compliance of aligned nanoscale polymer cylinders in confinement. *Langmuir* **20**(12), 5091–5099 (2004)
8. A. Laracuenta, M.J. Bronikowski, A. Gallagher, Chemical vapor deposition of nanometer-size aluminum features on silicon surfaces using an STM tip. *Appl. Surf. Sci.* **107**, 11–17 (1996)
9. G. Binnig, C.F. Quate, C. Gerber, Atomic force microscope. *Phys. Rev. Lett.* **56**(9), 930 (1986)
10. G. Binnig, H. Rohrer, Scanning tunneling microscopy. *IBM J. Res. Dev.* **44**(1–2), 279–293 (2000)
11. G. Binnig, et al., Surface studies by scanning tunneling microscopy. *Phys. Rev. Lett.* **49**(1), 57 (1982)
12. R.D. Piner, et al., “Dip-Pen” nanolithography. *Science* **283**(5402), 661–663 (1999)
13. S.Y. Chou, P.R. Krauss, P.J. Renstrom, Imprint lithography with 25-nanometer resolution. *Science* **272**(5258): 85–87 (1996)
14. J.A. Dagata, et al., Modification of hydrogen-passivated silicon by a scanning tunneling microscope operating in air. *Appl. Phys. Lett.* **56**(20), 2001–2003 (1990)
15. H.C. Day, D.R. Allee, Selective area oxidation of silicon with a scanning force microscope. *Appl. Phys. Lett.* **62**(21), 2691–2693 (1993)

16. K. Salaita, et al., Sub-100 nm, centimeter-scale, parallel dip-pen nanolithography. *Small* **1**(10), 940–945 (2005)
17. D. Bullen, et al., Parallel dip-pen nanolithography with arrays of individually addressable cantilevers. *Appl. Phys. Lett.* **84**(5), 789–791 (2004)
18. J. Haakeim, et al., Dip pen nanolithography (DPN): process and instrument performance with NanoInk's Nscriptor system. *Ultramicroscopy* **103**(2), 117–132 (2005)
19. Hong, S., J. Zhu, C.A. Mirkin, Multiple ink nanolithography: toward a multiple-pen nanoplotter. *Science* **286**(5439), 523–525 (1999)
20. S. Hong, C.A. Mirkin, A nanoplotter with both parallel and serial writing capabilities. *Science* **288**(5472), 1808–1811 (2000)
21. S.W. Lee, et al., Nanostructured polyelectrolyte multilayer organic thin films generated via parallel dip-pen nanolithography. *Adv. Mater.* **17**(22), 2749–2753 (2005)
22. L. Fu, et al., Nanopatterning of “Hard” magnetic nanostructures via dip-pen nanolithography and a sol-based ink. *Nano Lett.* **3**(6), 757–760 (2003)
23. J.-M. Nam, et al., Bioactive protein nanoarrays on nickel oxide surfaces formed by dip-pen nanolithography. *Angew. Chem. Int. Ed.* **43**(10), 1246–1249 (2004)
24. J. Jang, G.C. Schatz, M.A. Ratner, Capillary force on a nanoscale tip in dip-pen nanolithography. *Phys. Rev. Lett.* **90**(15), 156104 (2003)
25. P.E. Sheehan, L.J. Whitman, Thiol diffusion and the role of humidity in “Dip Pen Nanolithography”. *Phys. Rev. Lett.* **88**(15), 156104 (2002)
26. C.R. Lowe, Nanobiotechnology: the fabrication and applications of chemical and biological nanostructures. *Curr. Opin. Struct. Biol.* **10**(4), 428–434 (2000)
27. M.H. Hong, et al., Laser assisted surface nanopatterning. *Sensors Actuators A: Phys.* **108**(1–3), 69–74 (2003)
28. V. Grigalinas, et al., Laser pulse assisted nanoimprint lithography. *Thin Solid Films* **453–454**, 13–15 (2004)
29. A.A. Gorbunov, W. Pompe, Thin film nanoprocessing by laser/STM combination. *Physica Status Solidi (a)* **145**(2), 333–338 (1994)
30. S.M. Huang, et al., Pulsed laser-assisted surface structuring with optical near-field enhanced effects. *J. Appl. Phys.* **92**(5), 2495–2500 (2002)
31. M. Tortonese, Cantilevers and tips for atomic force microscopy. *Eng. Med. Biol. Mag., IEEE* **16**(2), 28–33 (1997)
32. B. Bhushan, *Scanning probe Microscopy in Nanoscience and Nanotechnology*, vol 14. Nanoscience and Technology (Springer, Berlin, 2010)

Scanning Probe Microscopy in Nanoscience and
Nanotechnology 3

Bhushan, B. (Ed.)

2013, XX, 630 p., Hardcover

ISBN: 978-3-642-25413-0